DFT Global Optimization of Gas-Phase Subnanometer Ru–Pt Clusters

Demiroglu, Ilker; Yao, Kezi; Hussein, Heider A; Johnston, Roy L.

DOI:
10.1021/acs.jpcc.6b11329

THE JOURNAL OF PHYSICAL CHEMISTRY C

Article

pubs.acs.org/JPCC

DFT Global Optimization of Gas-Phase Subnanometer Ru−Pt Clusters

Ilker Demiroglu, Kezi Yao, Heider A Hussein, and Roy L. Johnston*

School of Chemistry, University of Birmingham, Edgbaston, Birmingham B15 2TT, United Kingdom

Supporting Information

ABSTRACT: The global optimization of subnanometer Ru−Pt binary nanoalloys in the size range 2−8 atoms is systematically investigated using the Birmingham Parallel Genetic Algorithm (BPGA). The effect of size and composition on the structures, stabilities and mixing properties of Ru−Pt nanoalloys are discussed. The results revealed that the maximum mixing tendency is achieved for 40−50% Ru compositions. Global minimum structures show that the Ru atoms prefer to occupy central and core positions and maximize coordination number and the number of strong Ru−Ru bonds.

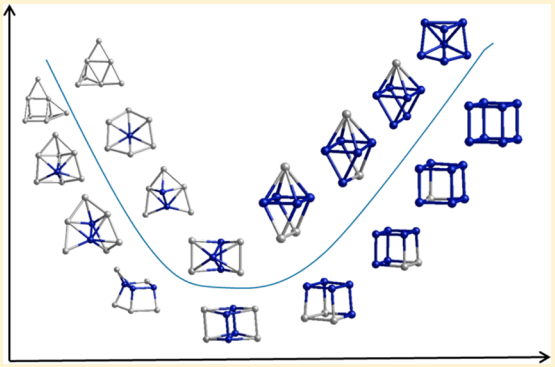

INTRODUCTION

Subnanometer noble metal clusters are of great importance due to their extraordinary structural and electronic properties, which are intermediate between atomic and nanoparticular systems.[1] The interest in subnanometer clusters is growing, especially in the field of catalysis, owing to recent experimental results suggesting high selectivity and activity toward specific reactions,[2−4] as well as advances in experimental procedures that allow size selectivity of subnanometer clusters.[5] One example is platinum (Pt) for which Vajda et al. have shown up to 2 orders of magnitude higher catalytic activities than previous Pt catalysts for the selective oxidative dehydrogenation of propane.[4]

Platinum is the key component in catalysts for low temperature methanol electro-oxidation, which is of great interest for direct methanol fuel cells.[6] However, pure platinum catalysts suffer from two main drawbacks: high cost and CO-poisoning.[7] Addition of another metal has been investigated, either to reduce the usage of comparatively expensive platinum or to improve CO tolerance. To optimize the catalysts, various bimetallic alloys have been tested for their catalytic properties, including Pt−Ni,[8] Pt−Co,[9] and Pt−Ru.[10−12] Among all these electrode materials, Pt−Ru catalysts have showed promising catalytic activities toward fuel cell applications[13,14] and higher CO tolerance.[15]

Pt in the bulk exhibits face-centered cubic (fcc) packing, while bulk Ru is hexagonal close-packed (hcp). The binary Ru−Pt phase diagram[16] suggests a fcc-type structure when Pt is above 40%, a hcp-type structure when Pt is below 20% and a coexisting hcp(Ru-rich)-fcc(Pt-rich) phase region for intermediate compositions. This phase diagram refers to solids at a temperature above 1000 °C, which is much higher than normal temperatures for Pt−Ru nanoalloy (NAs) synthesis and postsynthesis treatment. In addition, nanosize alloys sometimes show distinct structures from their bulk counterparts.[17,18] The atomic-scale structures of Pt−Ru nanoalloys, therefore, cannot be simply defined by their composition. Experimental conditions and synthetic methods also play important roles here. In the literature, composition-induced structural changes[19,20] were shown for Pt−Ru nanoalloys and mixed structures were obtained at low temperatures. Nevertheless, a high-temperature treatment after synthesis[21−23] showed Pt segregation to the surface, leading to "core-shell" particles and it has been shown that core−shell Ru@Pt nanoalloys have higher catalytic activity for CO oxidation than mixed Ru−Pt nanoparticles.[24]

Since the catalytic activities of nanoalloys are closely related to their sizes and structures, it is important to rationalize the relationship between structures and catalytic properties as well as mixing patterns at the nanoscale. Theoretical studies here can give an insight into size and structural effects on catalyst stability and activity. Although in the literature there have been a number of experimental and theoretical studies of pure subnanometer Ru[25−33] and Pt[4,34−39] clusters, to our knowledge there has been no theoretical study of subnanometer Ru−Pt alloys.

In this study, low energy structures of subnanometer Ru−Pt alloys have been systematically studied by global optimization at the DFT level within the Birmingham Parallel Genetic Algorithm (BPGA).

Special Issue: ISSPIC XVIII: International Symposium on Small Particles and Inorganic Clusters 2016

Received: November 10, 2016
Revised: December 22, 2016
Published: December 22, 2016

DOI: 10.1021/acs.jpcc.6b11329
J. Phys. Chem. C 2017, 121, 10773−10780

METHODOLOGY

The BPGA-DFT[40,41] approach was applied to obtain low energy structures of $(Ru,Pt)_N$ alloy clusters in the size range $N = 3-8$, as well as pure Ru_N and Pt_N clusters. This method is an open-source genetic algorithm, improving on the Birmingham Cluster Genetic Algorithm (BCGA), a genetic algorithm for determining the lowest energy structures of nanoparticles and nanoalloys directly at the DFT level.[42] BPGA employs a pool methodology[43] to evaluate structures in parallel instead of based on generations. In each run, multiple BPGA instances are implemented, and in each instance, a set of processes are run in parallel and independently. Initially a number of random structures (10 in this study) are generated and geometrically relaxed (by local energy minimization at the DFT level) to form a population. Once the local minimization of the initial pool structures has been completed, the crossover and mutation operations of the genetic algorithm begin for each instance. In each instance, either a pair of clusters are taken from the pool according to "roulette-wheel" selection[42] for the crossover operation to generate an "offspring" structure or a single cluster is taken for mutation. Offspring structures are produced through weighted crossover according to the Deaven and Ho "cut and splice" method.[44] Mutated clusters are either obtained by displacing some of the atoms randomly or swapping different types of atoms in alloy clusters. The newly generated structures are then locally minimized to compare with existing structures in the pool and the pool is updated whenever a new cluster is found that is lower in energy.

All the DFT-level local minimizations mentioned above were performed with a plane wave basis set, as implemented in the Vienna ab initio Simulation Package (VASP),[45−48] including spin polarization. Spin states are optimized within VASP independently for each generated structure from BPGA during global optimization. The exchange-correlation energy was calculated using the generalized gradient approximation (GGA), with the Perdew−Burke−Ernzerhof (PBE)[49] exchange-correlation functional. The interaction between valence electrons and ionic cores was described by the projector augmented wave (PAW) method.[50,51] Methfessel-Paxton smearing, with a sigma value of 0.01 eV, was implemented to improve convergence of metallic systems.[52]

For the comparison of the energetics of different composition nanoalloys, a mixing (or excess) energy term (Δ) was calculated, which is expressed as

$$\Delta = E_{tot}(A_mB_n) - m\frac{E_{tot}(A_{m+n})}{m+n} - n\frac{E_{tot}(B_{m+n})}{m+n}$$

where the total energy (E_{tot}) of the nanoalloy A_mB_n is compared to the pure metal clusters of A and B of the same size $(m + n)$. Hence, a negative value of Δ means an energy decrease upon mixing and therefore favorable mixing, whereas positive values indicate a demixing tendency.

The stability of each cluster, relative to its neighbors, is indicated by the second difference in energy Δ_2E, which is given by

$$\Delta_2E = E_{tot}(A_{N+1}) + E_{tot}(A_{N-1}) - 2E_{tot}(A_N)$$

where A is Ru or Pt, $E_{tot}(A_N)$ corresponds to the total energy of the N-atom cluster, and $E_{tot}(A_{N+1})$ and $E_{tot}(A_{N-1})$ are the neighboring clusters when increased one atom more and decreased one atom less, respectively.

The average binding energy per atom E_b is given by

$$E_b = -\frac{1}{N}[E_{tot}(A_mB_n) - mE_{tot}(A_1) - nE_{tot}(B_1)]$$

where m and n are the numbers of A and B atoms; $E_{tot}(A_1)$, and $E_{tot}(B_1)$ are the electronic energies of a single Ru or Pt atom; and N is the total number of atoms $(N = m + n)$.

RESULTS

Ru Clusters. The lowest energy structures obtained from global optimization for pure Ru_N clusters $(3 \le N \le 12)$ are shown in Figure 1. Overall, the global minimum clusters and their corresponding spin multiplicities are in good agreement with structures suggested in previous theoretical works.[25−29]

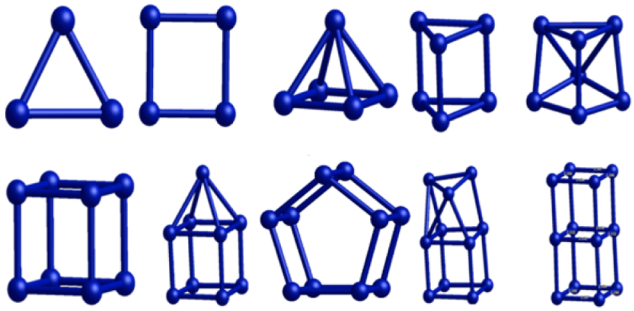

Figure 1. Global minima structures for pure Ru clusters $3 \le N \le 12$.

Ru_3 is an equilateral triangle (D_{3h}) and Ru_4 is also planar, while the larger sizes adopt 3D structures. Ru_4 is a rectangle with bond lengths of 2.24 and 2.15 Å. Ru_5 is a square pyramid (C_{4v}) and Ru_6 is a trigonal prism (D_{3h}) again with high symmetries as for Ru_3 and Ru_4 (see Table 1).

Table 1. Binding Energies E_b, Point Groups, and Spin Multiplicities $(2S + 1)$ for the Global Minimum Ru_N Clusters

cluster	point group	E_b (eV)	$(2S + 1)$
Ru_3	D_{3h}	2.66	7
Ru_4	D_{2h}	3.24	1
Ru_5	C_{4v}	3.50	1
Ru_6	D_{3h}	3.78	5
Ru_7	C_s	3.97	7
Ru_8	O_h	4.34	5
Ru_9	C_{4v}	4.26	9
Ru_{10}	D_{5h}	4.36	1
Ru_{11}	C_1	4.37	1
Ru_{12}	D_{4h}	4.54	5

The first low symmetry structure is Ru_7 with point group C_s, which is in agreement with the cationic Ar-tagged species Ru_7Ar^+ observed in gas phase experiments.[33] Ru_8 is found to be cubic (with full O_h symmetry), while Ru_9 has an additional Ru atom capping a face of the cube (C_{4v} symmetry). These structures are in agreement with recent experiments on both cationic[33] and anionic[28] clusters, which indicate the occurrence of cubic structures for certain nuclearities. The lowest energy structure for Ru_{10} is found to be pentagonal prism (D_{5h}), as in previous theoretical studies.[25,27,29] However, a doubly capped cube has been shown to give a better fit to electron diffraction measurements for anionic Ru_{10}^- clusters.[28] The lowest energy structure for Ru_{11} is found to be a cube with three atoms on the top face, missing one atom to complete the double cube, leading to the lowest (C_1) symmetry. Ru_{12} is found to be a

DOI: 10.1021/acs.jpcc.6b11329
J. Phys. Chem. C 2017, 121, 10773−10780

double cube (D_{4h}) with the edges of the middle square being shorter than the top and bottom layers which are equal. Most of our results agree well with anionic or cationic clusters investigated experimentally, except for Ru_{10}^- and Ru_{12}^-, in which the configurations that fit the experimental results best have lower symmetry point groups than we have found for the neutral clusters. When we compared the effect of charge for Ru_8 (see Supporting Information, Figure 1), while Ru_8^- preserved the perfect cubic structure, Ru_8^+ distorted into a squashed cube (with D_{4h} symmetry).

According to Table 1, the binding energies of the clusters increase with increasing cluster size, as expected, to converge on the bulk cohesive energy (calculated value = 6.78 eV). However, the higher binding energy calculated for Ru_8 than Ru_9 indicates the extra stability of the cubic structure of Ru_8. This extra stability is also confirmed by fitting binding energies as a function of $n^{1/3}$ for small clusters (see Supporting Information, Figure 2). Although the cubic Ru_8 has the highest positive residual, indicating a "magic" size, larger cubic clusters Ru_{11} and Ru_{12} have negative residuals, indicating reduced relative stability.

Pt Clusters. Figure 2 shows the lowest energy structures of pure Pt_N clusters ($3 \le N \le 10$). In addition to the equilateral

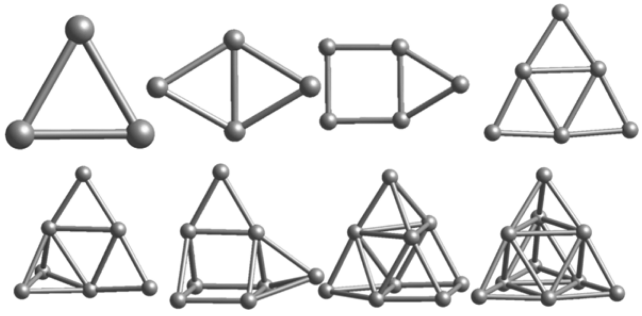

Figure 2. Global minima structures for pure Pt clusters $3 \le N \le 10$.

triangular Pt_3 (D_{3h}), the lowest isomer of Pt_6 is also planar (D_{3h}), while Pt_4 has a slightly bent rhombus configuration and Pt_5 is an edge-bridged square with a slight bending out of the square plane. The global minimum configuration of Pt_7 is based on the planar structure of Pt_6, with an outer triangle capped to generate a 3D structure (with C_s symmetry).

For both Pt_8 and Pt_9, global optimization leads to 3D structures, which are the same structures previously predicted[35] for Pt_8^+ and Pt_9^+ cations, though there are quasi-2D structures which are nearly degenerate with the 3D isomers. The 3D Pt_8 and Pt_9 structures are both based on the structure of Pt_6 mentioned above, with the planar structure of Pt_6 capped to form 3D triangular structures tending toward a tetrahedral structure. The 2D Pt_9 isomer is a 3×3 square lattice.[34−36] Pt_{10} is found to be the tetrahedral (T_d) structure, corresponding to a small fragment of fcc packing.

Overall, our low energy structures and their corresponding spin multiplicities compare well with previous studies.[34−36,38,39] For the high symmetry structures of Pt_3, Pt_6, and Pt_{10} (see Table 2), all previous studies have shown the same lowest energy structures, while nonglobal optimization studies[34,36,38,39] did not considered some of the lowest energy structures for other sizes. However, most of lowest energy isomers presented here are in good agreement with a previous global optimization study.[35] Although it has been reported that all global minima up

Table 2. Binding Energies E_b, Point Groups, and Spin Multiplicities $(2S + 1)$ for the Global Minimum Pt_N Clusters

cluster	point group	E_b (eV)	$(2S + 1)$
Pt_3	D_{3h}	2.51	1
Pt_4	C_{2v}	2.80	5
Pt_5	C_s	3.05	3
Pt_6	D_{3h}	3.31	3
Pt_7	C_s	3.41	5
Pt_8 (2D)	C_1	3.51	3
Pt_8 (3D)	C_s	3.51	1
Pt_9 (2D)	D_{4h}	3.65	5
Pt_9 (3D)	C_{2v}	3.65	7
Pt_{10}	T_d	3.80	9

to Pt_9 are planar for neutral Pt clusters, here it is shown that 3D clusters become competitive after Pt_7, that is, having almost the same binding energies as their planar counterparts. As for Ru clusters, binding energies of Pt clusters increase with increasing cluster size to converge on the bulk cohesive energy (calculated value = 5.58 eV) and the fit to $n^{-1/3}$ reveals the extra stability of Pt_3, Pt_6, and Pt_{10} clusters with positive residuals (see Supporting Information, Figure 3).

Ru−Pt Clusters. The global minima for all compositions of Ru_mPt_n clusters for $3 \le m + n \le 8$, are shown in Figure 3. For all sizes and compositions, due to the high cohesive energy of Ru (as shown in Table 3), the Ru atoms prefer to occupy core-like positions with higher coordination numbers. Moreover, when there is more than one Ru atom, Ru atoms tend to occupy adjacent positions, due to the stronger Ru−Ru bonds.

All the favored structures of Ru_mPt_1 are similar to the pure Ru clusters of the same size (Ru_{m+1}), except for Ru_6Pt_1, in which the Pt atom caps one of the square faces of the trigonal prism structure of Ru_6. Ru_1Pt_3, Ru_1Pt_4, and Ru_1Pt_5 resemble the pure Pt clusters, while Ru_1Pt_7 and Ru_1Pt_6 both possess a Ru atom with high coordination number and differ significantly from the corresponding pure-Pt clusters. In Ru_1Pt_2, the triangle opens up and the Pt−Pt distance becomes 3.77 Å from the value of 2.46 Å in Pt_3, while the Pt−Ru distances are 2.23 Å. In contrast, for Ru_2Pt_1, the Ru−Ru distance is smaller (2.12 Å) than Ru_3 (2.24 Å), while the Ru−Pt distances are 2.48 Å. For $(Ru,Pt)_4$, the rhombus structure of Pt_4 is preserved until all but one Pt atom is replaced with Ru, at which point the structure converts to a distorted square structure similar to Ru_4. Similarly, for $(Ru,Pt)_5$ and $(Ru,Pt)_6$, pure Pt structures are preserved until more than 50% replacement of Ru, while an intermediate nonplanar trapezoidal structure is observed for Ru_3Pt_2 before adopting the square pyramidal pure Pt structure. Ru_4Pt_2 is an edge-bridged square pyramid, which has same coordination numbers (three and four) as Ru_3Pt_2.

For $(Ru,Pt)_7$, the structure of Ru_1Pt_6 has a Ru atom surrounded by six Pt atoms, so that the Ru atom obtain the maximum coordination number. In this structure, six Pt atoms around the Ru atoms form a chairlike configuration, in which the Ru atom sits ~0.5 Å out of the vertical plane. In Ru_2Pt_5, the additional Ru atom moves toward to the center and binds to two extra Pt atoms while displacing the central Ru atom out of the plane. Ru_3Pt_4 is two square pyramids sharing a triangular Ru_3 face, ensuring the three Ru atoms are bonded together and have high coordination numbers. The structures of Ru_4Pt_3 and Ru_5Pt_2 resemble the Ru_6Pt_1 structure, corresponding to a trigonal prism with a square Ru_4 face capped by a Pt atom. For $(Ru,Pt)_8$, when the composition is 50%, the structure is a

DOI: 10.1021/acs.jpcc.6b11329
J. Phys. Chem. C 2017, 121, 10773−10780

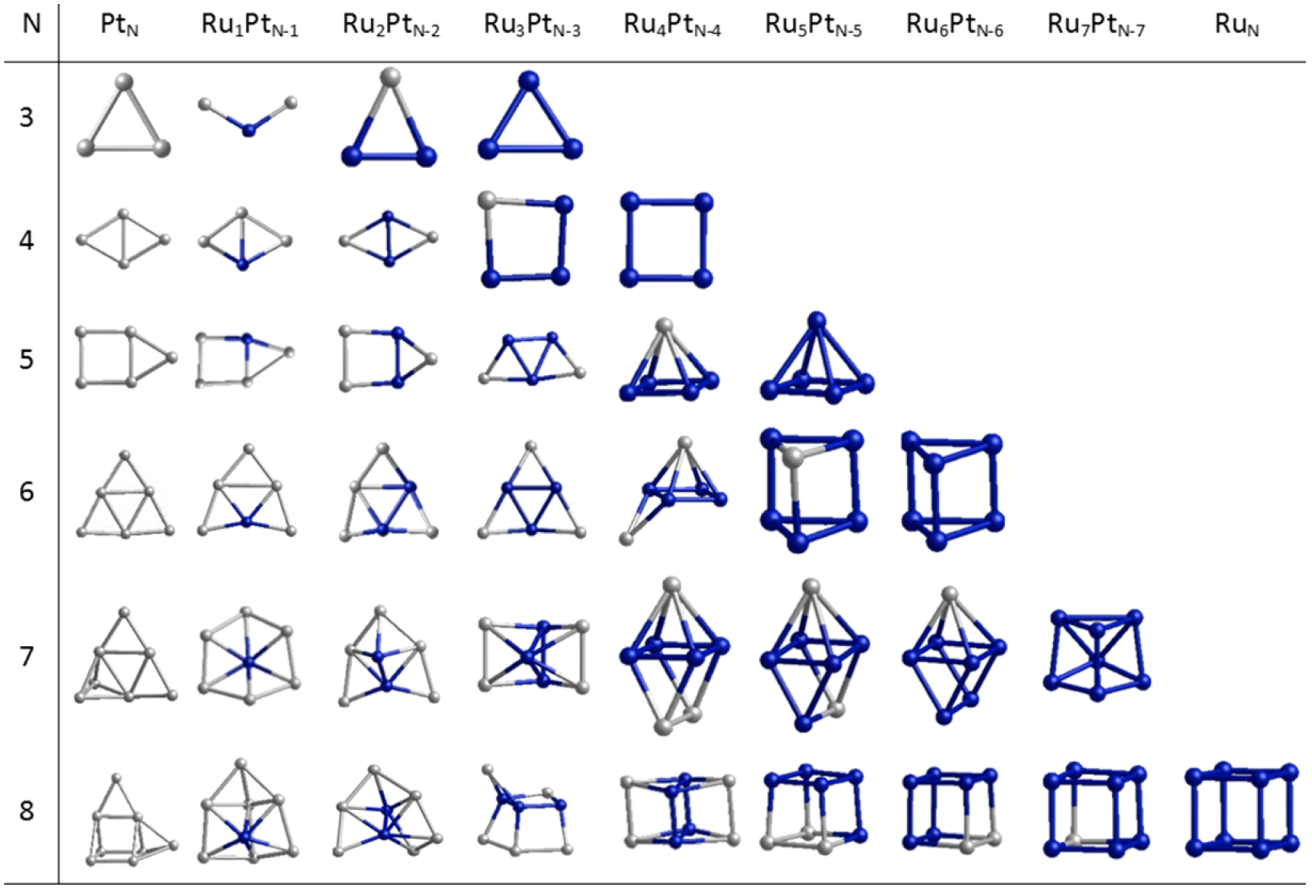

Figure 3. Global minima structures for all composition of Ru−Pt clusters $3 \leq N \leq 8$.

Table 3. Bond Lengths and Binding Energies of Ru−Ru, Ru−Pt, and Pt−Pt Dimers, As Well As Cohesive Energies of Bulk Ru and Pt

dimer	bond length (Å)	binding energy (eV)
Ru−Ru	2.04	2.00
Ru−Pt	2.25	2.13
Pt−Pt	2.32	1.94
bulk	bond length (Å)	cohesive energy (eV)
Ru	2.65 and 2.72	6.78
Ru (exp.)[53]	2.64 and 2.71	6.74
Pt	2.80	5.58
Pt (exp.)[53]	2.77	5.84

distorted cube, corresponding to two trigonal prisms sharing a square Ru_4 face. As the Ru percentage increases, the structure becomes more cubic.

Apart from sizes n = 4 and 5, pure Ru_n clusters have higher spin multiplicities than pure Pt_n clusters (see Tables 1 and 2). Upon alloying (Table 4), as Ru replaces Pt, spin multiplicities increase in general for $(RuPt)_n$ clusters up to 40% Ru composition (see Supporting Information, Figure 4). For $(Ru,Pt)_4$, $(Ru,Pt)_5$, and $(Ru,Pt)_6$, spin multiplicities on Ru doping of the Pt structure start to decrease when the Ru structure starts to dominate the alloy geometry. For $(Ru,Pt)_7$, spin multiplicities do not follow the trend as all the alloy structures are significantly different than the pure Ru or pure Pt geometries. For $(Ru,Pt)_8$, spin multiplicities become maximal as the cubic Ru structure dominates the alloy geometry, but decreases for pure Ru.

Energetic Analysis. The relative stabilities of the clusters can be studied by calculating the second difference in energy ($\Delta_2 E$), which indicates the stability of an N atom cluster with respect to neighboring sizes. Figure 4 shows the plot of second difference in energy as a function of cluster size for pure Ru and pure Pt clusters, respectively. The significant positive peaks indicate the relatively stable clusters.

Figure 4 reveals that Ru_8 and Pt_6 clusters are significantly more stable relative to their neighbors, suggesting they are "magic" sizes in the considered subnanometer regime. However, note that the energetic range for Ru clusters (approximately 5.0 eV) is larger than for Pt clusters (approximately 1.0 eV) and also the binding energy versus cluster size fit (see Supporting Information, Figure 3) reveals higher stability for tetrahedral Pt_{10} than planar Pt_6. For Ru clusters, the second difference energies also reveal an even−odd alternation, where even number of Ru clusters are more stable than the neighboring odd number clusters.

The effect of mixing Ru with Pt in small clusters is studied by calculating the mixing energy, Δ. Mixing energies as a function to the number of Ru atoms for all compositions of $3 \leq m + n \leq 8$ for Ru_mPt_n clusters are plotted in Figure 5. Negative values of mixing energy indicate a favorable mixing, whereas demixing is represented by positive values.

For $(Ru,Pt)_3$, both alloy composition shows a mixing tendency. All compositions for $(Ru,Pt)_4$ clusters also favor mixing except for Ru_3Pt_1, in which the dopant Pt atom distorts the rectangular structure of Ru. For $(Ru,Pt)_5$ clusters, high Pt compositions show more negative mixing energies than high Ru compositions, and the mixing tendency is maximum for 40%

DOI: 10.1021/acs.jpcc.6b11329
J. Phys. Chem. C 2017, 121, 10773−10780

Table 4. Binding Energies E_b, Point Groups, and Spin Multiplicities $(2S + 1)$ for the Global Minimum Ru_mPt_n Clusters

cluster	point group	E_b (eV)	$(2S + 1)$
Ru_1Pt_2	C_{2v}	2.64	5
Ru_2Pt_1	C_{2v}	2.70	5
Ru_1Pt_3	C_1	3.00	7
Ru_2Pt_2	C_{2v}	3.18	7
Ru_3Pt_1	C_{2v}	3.10	3
Ru_1Pt_4	C_1	3.20	5
Ru_2Pt_3	C_s	3.34	7
Ru_3Pt_2	C_1	3.37	7
Ru_4Pt_1	C_{4v}	3.43	5
Ru_1Pt_5	C_{2v}	3.40	3
Ru_2Pt_4	C_1	3.52	7
Ru_3Pt_3	C_s	3.59	5
Ru_4Pt_2	C_s	3.63	5
Ru_5Pt_1	C_s	3.71	7
Ru_1Pt_6	C_s	3.53	5
Ru_2Pt_5	C_s	3.65	3
Ru_3Pt_4	C_{2v}	3.76	3
Ru_4Pt_3	C_{2v}	3.82	3
Ru_5Pt_2	C_s	3.87	5
Ru_6Pt_1	C_{2v}	3.94	3
Ru_1Pt_7	C_s	3.63	5
Ru_2Pt_6	C_1	3.74	5
Ru_3Pt_5	C_1	3.83	3
Ru_4Pt_4	D_{2h}	3.99	3
Ru_5Pt_3	C_s	4.05	7
Ru_6Pt_2	C_{2v}	4.17	7
Ru_7Pt_1	C_{3v}	4.26	7

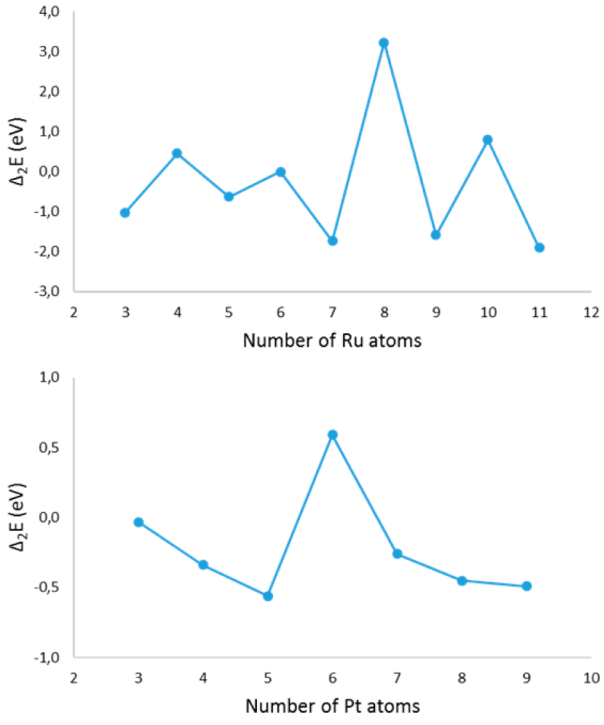

Figure 4. Second difference in energy $(\Delta_2 E)$ of Ru (top) and Pt clusters (bottom) with respect to the number of atoms.

Ru. Similarly, the Ru_2Pt_4 composition is found to have the maximum mixing tendency for $(Ru,Pt)_6$ clusters, which has a

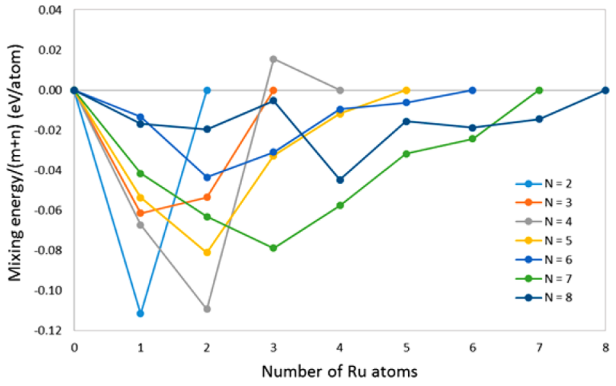

Figure 5. Mixing energies as a function of number of Ru atoms for all compositions of $3 \leq m + n \leq 8$ for Ru_mPt_n clusters.

33% Ru composition, while the second best was found for 50% composition, whereas for other compositions the mixing energies were found to be close to zero.

For $(Ru,Pt)_7$, the Ru_3Pt_4 structure has the maximum mixing tendency, followed by the two neighboring compositions. Again, in $(Ru,Pt)_8$, the 50% configuration favors mixing more than the other compositions. Pt-rich compositions for $(Ru,Pt)_8$ are found to have reduced mixing tendencies than the Ru-rich configurations because of the magic size of pure Ru_8. The largest mixing energy is found for Ru_1Pt_1, and Ru_2Pt_2, followed by Ru_1Pt_2, Ru_2Pt_3, and Ru_3Pt_4. For $(Ru,Pt)_6$ clusters mixing tendency is lower than for $(Ru,Pt)_5$ and $(Ru,Pt)_7$, in general, because of the magic size of pure Pt_6, as in the Ru_8 case.

Figure 5 also reveals that alloy clusters with even numbers of Ru atoms usually lie below the line connecting its neighbors. That is to say, clusters with even numbers of Ru atoms favor mixing more than the adjacent clusters, which have odd number of Ru atoms. This also fits with the even−odd stability order of pure Ru clusters (see Figure 4); however, the trend is not as clear as for the pure Ru clusters.

The binding energy per atom (E_b), which is related to the stability of nanoclusters, is shown in Figure 6. According to the

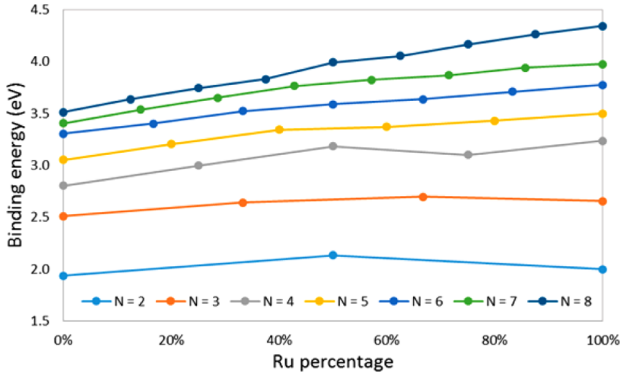

Figure 6. Binding energies of Ru−Pt clusters for each size $N = 2$−8 against the Ru composition.

figure, binding energy increases with increasing cluster size. The binding energy also increases with increasing Ru composition except for the Ru dimer, Ru_3, and Ru_3Pt_1, which is in agreement with the higher cohesive energy of Ru than Pt. From the binding energy plot, it can be seen that values for 40−50% Ru compositions are slightly higher than the connecting lines, which indicates higher stabilities at these compositions. Mixing

DOI: 10.1021/acs.jpcc.6b11329
J. Phys. Chem. C 2017, 121, 10773−10780

energy and second difference in energy values for nanoalloy clusters also confirm this trend. In the second difference energy plot in Figure 7, there are positive peaks for 50% Ru compositions of $(Ru,Pt)_4$ and $(Ru,Pt)_8$, while the peaks are at around 40% Ru composition for $(Ru,Pt)_5$, $(Ru,Pt)_6$, and $(Ru,Pt)_7$.

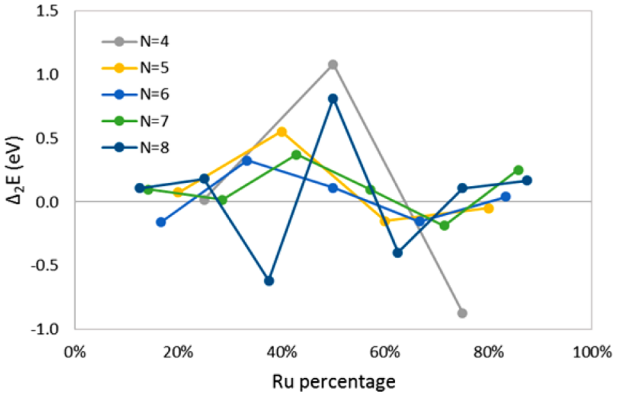

Figure 7. Second difference in energy (Δ_2E) of $(RuPt)_N$ clusters for N = 4–8 with respect to Ru composition.

HOMO–LUMO gaps are often used as an indicator for the structural stabilities of small clusters, with higher HOMO–LUMO gaps usually indicating higher stabilities. However, our calculations revealed that the HOMO–LUMO gaps are smallest for the "magic" sizes of Pt_6 and Ru_8 for pure metal clusters (see Supporting Information, Figure 5). For alloy clusters, higher HOMO–LUMO gaps correlate well with the suggested high stable compositions of $(Ru,Pt)_4$, $(Ru,Pt)_6$, and $(Ru,Pt)_7$. However, smaller HOMO–LUMO gaps are found for $(Ru,Pt)_5$ and $(Ru,Pt)_8$.

Although the trends discussed here only consider the lowest energy (global minimum) clusters, global optimization calculations also revealed several low-lying isomers of alloy clusters. For the higher stability compositions for each size (Ru_2Pt_2, Ru_2Pt_3, Ru_2Pt_4, Ru_3Pt_4, and Ru_4Pt_4), no low-lying isomers were found within a binding energy range of 0.3 eV. Several low-lying isomers are found, however, for less stable alloy clusters. For example, for $(Ru,Pt)_6$, low lying isomers found for Ru_3Pt_3 and Ru_4Pt_2 with 0.03 eV energy difference with corresponding global minima structures (see Supporting Information, Table 3). While Ru_3Pt_3 isomer is a distorted structure of global minima Ru_3Pt_3, Ru_4Pt_2 isomer is again an edge-capped square pyramid structure as in the global minimum Ru_4Pt_2, only with a different edge capped. Similarly for $(Ru,Pt)_7$, low-lying isomers are found for Ru_4Pt_3 and Ru_5Pt_2, which have the same geometric structure as the highly stable Ru_3Pt_4 composition.

Bader charge analysis[54] shows that there is a 0.41 e^- charge transfer from Ru to Pt in the RuPt dimer. For Ru_mPt_1 clusters, calculated Ru–Pt charge transfers are between 0.4 and 0.5 e^-, while for Ru_1Pt_n clusters there is higher charge transfer (between 0.7 and 0.9 e^-). Charge transfer also increases as the composition get closer to 50% for alloy clusters (see Supporting Information, Figure 6). Ru–Pt charge transfer may play a role in strengthening Ru–Pt interactions and may also contribute to the stabilization of cluster isomers with Ru atoms occupying central positions, surrounded by Pt.

CONCLUSIONS

We have performed a computational study of Ru–Pt nanoalloys ranging from 3 to 8 atoms and compared them with pure Ru and Pt clusters in the same size range. The structural properties and energetics of bimetallic Ru–Pt nanoalloys have been studied within the framework of the BPGA-DFT approach that performs a global optimization search for the lowest energy configuration for each size and composition directly at the DFT level.

The calculations reveal that Ru atoms prefer central and adjacent positions due to stronger Ru–Ru bonds than Pt–Pt bonds, while the Pt atoms occupy peripheral positions. This, together with shorter Ru–Ru bond lengths, also predicts that "core-shell" Ru@Pt structures would become thermodynamically more stable as the cluster size increases. Energetic analysis shows that Ru compositions of 40–50% exhibit more favorable mixing than Ru-rich or Pt-rich compositions.

In future work, this study will be extended to larger bimetallic Ru–Pt nanoalloys, to investigate core–shell Ru–Pt structure formation.

ASSOCIATED CONTENT

Supporting Information

The Supporting Information is available free of charge on the ACS Publications website at DOI: 10.1021/acs.jpcc.6b11329.

All the Cartesian coordinates and energy values for considered subnanometer clusters (PDF).

AUTHOR INFORMATION

Corresponding Author

*E-mail: r.l.johnston@bham.ac.uk. Tel.: +44 121 414 7477.

ORCID

Ilker Demiroglu: 0000-0001-7801-4566

Roy L. Johnston: 0000-0003-4019-9280

Notes

The authors declare no competing financial interest.

ACKNOWLEDGMENTS

We acknowledge the Engineering and Physical Sciences Research Council, U.K. (EPSRC), for funding under Critical Mass Grant EP/J010804/1 "TOUCAN: Towards an Understanding of Catalysis on Nanoalloys". Calculations were performed on the following HPC facilities: The University of Birmingham BlueBEAR facility (see http://www.bear.bham.ac.uk/bluebear for more details) and the UK's national HPC facility, ARCHER, both via membership of the UK's HPC Materials Chemistry Consortium, which is funded by EPSRC (EP/L000202), and via the TOUCAN Grant. I.D. and K.Y. also thank Zhen Yao for her valuable help.

REFERENCES

(1) Ferrando, R.; Jellinek, J.; Johnston, R. L. Nanoalloys: From Theory to Applications of Alloy Clusters and Nanoparticles. *Chem. Rev.* **2008**, *108*, 845–910.

(2) Lei, Y.; Mehmood, F.; Lee, S.; Greeley, J.; Lee, B.; Seifert, S.; Winans, R. E.; Elam, J. W.; Meyer, R. J.; Redfern, P. C.; et al. Increased Silver Activity for Direct Propylene Epoxidation via Subnanometer Size Effects. *Science (Washington, DC, U. S.)* **2010**, *328*, 224–228.

(3) Oliver-Meseguer, J.; Cabrero-Antonino, J. R.; Domínguez, I.; Leyva-Pérez, A.; Corma, A. Small Gold Clusters Formed in Solution Give Reaction Turnover Numbers of 10(7) at Room Temperature. *Science* **2012**, *338*, 1452.

(4) Vajda, S.; Pellin, M. J.; Greeley, J. P.; Marshall, C. L.; Curtiss, L. A.; Ballentine, G. A.; Elam, J. W.; Catillon-Mucherie, S.; Redfern, P. C.; Mehmood, F.; et al. Subnanometre Platinum Clusters as Highly Active and Selective Catalysts for the Oxidative Dehydrogenation of Propane. *Nat. Mater.* **2009**, *8*, 213−216.
(5) Lu, Y.; Chen, W. Sub-Nanometre Sized Metal Clusters: From Synthetic Challenges to the Unique Property Discoveries. *Chem. Soc. Rev.* **2012**, *41*, 3594−3623.
(6) Steele, B. C. H.; Heinzel, A. Materials for Fuel-Cell Technologies. *Nature* **2001**, *414*, 345−352.
(7) Lemons, R. A. Fuel Cells for Transportation. *J. Power Sources* **1990**, *29*, 251−264.
(8) Mathiyarasu, J.; Remona, A. M.; Mani, A.; Phani, K. L. N.; Yegnaraman, V.; Phani, M. K. L. N. Exploration of Electrodeposited Platinum Alloy Catalysts for Methanol Electro-Oxidation in 0.5 M H_2SO_4: Pt-Ni System. *J. Solid State Electrochem.* **2004**, *8*, 968−975.
(9) Antolini, E.; Salgado, J. R. C.; Gonzalez, E. R. The Stability of Pt-M (M = First Row Transition Metal) Alloy Catalysts and Its Effect on the Activity in Low Temperature Fuel Cells. A Literature Review and Tests on a Pt-Co Catalyst. *J. Power Sources* **2006**, *160*, 957−968.
(10) Watanabe, M.; Motoo, S. Electrocatalysis by Ad-Atoms. *J. Electroanal. Chem. Interfacial Electrochem.* **1975**, *60*, 275−283.
(11) Watanabe, M.; Uchida, M.; Motoo, S. Preparation of Highly Dispersed Pt + Ru Alloy Clusters and the Activity for the Electrooxidation of Methanol. *J. Electroanal. Chem. Interfacial Electrochem.* **1987**, *229*, 395−406.
(12) Chu, D. Methanol Electro-Oxidation on Unsupported Pt-Ru Alloys at Different Temperatures. *J. Electrochem. Soc.* **1996**, *143*, 1685.
(13) Aricò, A. S.; Srinivasan, S.; Antonucci, V. DMFCs: From Fundamental Aspects to Technology Development. *Fuel Cells* **2001**, *1*, 133−161.
(14) Liu, H.; Song, C.; Zhang, L.; Zhang, J.; Wang, H.; Wilkinson, D. P. A Review of Anode Catalysis in the Direct Methanol Fuel Cell. *J. Power Sources* **2006**, *155*, 95−110.
(15) Brankovic, S. R.; Wang, J. X.; Adzic, R. R. Pt Submonolayers on Ru Nanoparticles - A Novel Low Pt Loading, High CO Tolerance Fuel Cell Electrocatalyst. *Electrochem. Solid-State Lett.* **2001**, *4*, A217−A220.
(16) Massalski, T. B.; Okamoto, H.; Subramanian, P. R. *Binary Alloy Phase Diagrams*; ASM International: OH, 1990.
(17) Busani, R.; Folkers, M.; Cheshnovsky, O. Direct Observation of Band-Gap Closure in Mercury Clusters. *Phys. Rev. Lett.* **1998**, *81*, 3836−3839.
(18) Jellinek, J.; Acioli, P. H. Magnesium Clusters: Structural and Electronic Properties and the Size-Induced Nonmetal-to-Metal Transition. *J. Phys. Chem. A* **2002**, *106*, 10919−10925.
(19) Pan, C.; Dassenoy, F.; Casanove, M.-J.; Philippot, K.; Amiens, C.; Lecante, P.; Mosset, A.; Chaudret, B. A New Synthetic Method toward Bimetallic Ruthenium Platinum Nanoparticles; Composition Induced Structural Changes. *J. Phys. Chem. B* **1999**, *103*, 10098−10101.
(20) Liu, Z.; Ling, X. Y.; Su, X.; Lee, J. Y. Carbon-Supported Pt and PtRu Nanoparticles as Catalysts for a Direct Methanol Fuel Cell. *J. Phys. Chem. B* **2004**, *108*, 8234−8240.
(21) Nashner, M. S.; Frenkel, A. I.; Somerville, D.; Hills, C. W.; Shapley, J. R.; Nuzzo, R. G. Core Shell Inversion during Nucleation and Growth of Bimetallic Pt/Ru Nanoparticles. *J. Am. Chem. Soc.* **1998**, *120*, 8093−8101.
(22) Jeon, T.-Y.; Lee, K.-S.; Yoo, S. J.; Cho, Y.-H.; Kang, S. H.; Sung, Y.-E. Effect of Surface Segregation on the Methanol Oxidation Reaction in Carbon-Supported Pt-Ru Alloy Nanoparticles. *Langmuir* **2010**, *26*, 9123−9129.
(23) Zhang, H.; Zheng, Z.; Ma, C.; Zheng, J.; Zhang, N.; Li, Y.; Chen, B. H. Tuning Surface Properties and Catalytic Performances of Pt-Ru Bimetallic Nanoparticles by Thermal Treatment. *ChemCatChem* **2015**, *7*, 245−249.
(24) Alayoglu, S.; Nilekar, A. U.; Mavrikakis, M.; Eichhorn, B. Ru−Pt Core−shell Nanoparticles for Preferential Oxidation of Carbon Monoxide in Hydrogen. *Nat. Mater.* **2008**, *7*, 333−338.
(25) Aguilera-Granja, F.; Balbás, L. C.; Vega, A. Study of the Structural and Electronic Properties of RhN and RuN Clusters (N < 20) within the Density Functional Theory. *J. Phys. Chem. A* **2009**, *113*, 13483−13491.
(26) Bae, Y.-C.; Osanai, H.; Kumar, V.; Kawazoe, Y. Atomic Structures and Magnetic Behavior of Small Ruthenium Clusters. *Mater. Trans.* **2005**, *46*, 159−162.
(27) Li, S.; Li, H.; Liu, J.; Xue, X.; Tian, Y.; He, H.; Jia, Y. Structural and Electronic Properties of Run Clusters (n = 2−14) Studied by First-Principles Calculations. *Phys. Rev. B: Condens. Matter Mater. Phys.* **2007**, *76*, 45410.
(28) Waldt, E.; Hehn, A.-S.; Ahlrichs, R.; Kappes, M. M.; Schooss, D. Structural Evolution of Small Ruthenium Cluster Anions. *J. Chem. Phys.* **2015**, *142*, 24319.
(29) Zhang, W.; Zhao, H.; Wang, L. The Simple Cubic Structure of Ruthenium Clusters. *J. Phys. Chem. B* **2004**, *108*, 2140−2147.
(30) Kerpal, C.; Harding, D. J.; Lyon, J. T.; Meijer, G.; Fielicke, A. N2 Activation by Neutral Ruthenium Clusters. *J. Phys. Chem. C* **2013**, *117*, 12153−12158.
(31) Lang, S. M.; Bernhardt, T. M.; Krstič, M.; Bonačič-Koutecký, V. The Origin of the Selectivity and Activity of Ruthenium-Cluster Catalysts for Fuel-Cell Feed-Gas Purification: A Gas-Phase Approach. *Angew. Chem., Int. Ed.* **2014**, *53*, 5467−5471.
(32) Shetty, S.; Jansen, A. P. J.; van Santen, R. A. Magnetic, Bonding and Structural Behavior of Ru12 and Ru13 Clusters: Is Ru12 Magic? *J. Mol. Struct.: THEOCHEM* **2010**, *954*, 109−114.
(33) Kerpal, C.; Harding, D. J.; Rayner, D. M.; Lyon, J. T.; Fielicke, A. Far-IR Spectra and Structures of Small Cationic Ruthenium Clusters: Evidence for Cubic Motifs. *J. Phys. Chem. C* **2015**, *119*, 10869−10875.
(34) Bhattacharyya, K.; Majumder, C. Growth Pattern and Bonding Trends in Ptn (N = 2−13) Clusters: Theoretical Investigation Based on First Principle Calculations. *Chem. Phys. Lett.* **2007**, *446*, 374−379.
(35) Chaves, A. S.; Rondina, G. G.; Piotrowski, M. J.; Tereshchuk, P.; Da Silva, J. L. F. The Role of Charge States in the Atomic Structure of Cun and Ptn (N = 2−14 Atoms) Clusters: A DFT Investigation. *J. Phys. Chem. A* **2014**, *118*, 10813−10821.
(36) Kumar, V.; Kawazoe, Y. Evolution of Atomic and Electronic Structure of Pt Clusters: Planar, Layered, Pyramidal, Cage, Cubic, and Octahedral Growth. *Phys. Rev. B: Condens. Matter Mater. Phys.* **2008**, *77*, 205418.
(37) Negreiros, F. R.; Fabris, S. Role of Cluster Morphology in the Dynamics and Reactivity of Subnanometer Pt Clusters Supported on Ceria Surfaces. *J. Phys. Chem. C* **2014**, *118*, 21014−21020.
(38) Nie, A.; Wu, J.; Zhou, C.; Yao, S.; Luo, C.; Forrey, R. C.; Cheng, H. Structural Evolution of Subnano Platinum Clusters. *Int. J. Quantum Chem.* **2007**, *107*, 219−224.
(39) Xiao, L.; Wang, L. Structures of Platinum Clusters: Planar or Spherical. *J. Phys. Chem. A* **2004**, *108*, 8605−8614.
(40) JBADavis/BPGA — Bitbucket; https://bitbucket.org/JBADavis/bpga/ (accessed March 15, 2016).
(41) Davis, J.; Shayeghi, A.; Horswell, S. L.; Johnston, R. L. The Birmingham Parallel Genetic Algorithm and Its Application to the Direct DFT Global Optimisation of IrN (N = 10 − 20) Clusters. *Nanoscale* **2015**, *7*, 14032−14038.
(42) Johnston, R. L. Evolving Better Nanoparticles: Genetic Algorithms for Optimising Cluster Geometries. *Dalt. Trans.* **2003**, *70*, 4193.
(43) Bandow, B.; Hartke, B. Larger Water Clusters with Edges and Corners on Their Way to Ice: Structural Trends Elucidated with an Improved Parallel Evolutionary Algorithm. *J. Phys. Chem. A* **2006**, *110*, 5809−5822.
(44) Deaven, D. M.; Ho, K. M. Molecular Geometry Optimization with a Genetic Algorithm. *Phys. Rev. Lett.* **1995**, *75*, 288−291.
(45) Kresse, G.; Furthmüller, J. Efficiency of Ab-Initio Total Energy Calculations for Metals and Semiconductors Using a Plane-Wave Basis Set. *Comput. Mater. Sci.* **1996**, *6*, 15−50.

DOI: 10.1021/acs.jpcc.6b11329
J. Phys. Chem. C 2017, 121, 10773−10780

(46) Kresse, G.; Furthmüller, J. Efficient Iterative Schemes for Ab Initio Total-Energy Calculations Using a Plane-Wave Basis Set. *Phys. Rev. B: Condens. Matter Mater. Phys.* **1996**, *54*, 11169−11186.
(47) Kresse, G.; Hafner, J. Ab Initio Molecular-Dynamics Simulation of the Liquid-Metalamorphous- Semiconductor Transition in Germanium. *Phys. Rev. B: Condens. Matter Mater. Phys.* **1994**, *49*, 14251−14269.
(48) Kresse, G.; Hafner, J. Ab Initio Molecular Dynamics for Liquid Metals. *Phys. Rev. B: Condens. Matter Mater. Phys.* **1993**, *47*, 558−561.
(49) Perdew, J. P.; Burke, K.; Ernzerhof, M. Generalized Gradient Approximation Made Simple. *Phys. Rev. Lett.* **1996**, *77*, 3865−3868.
(50) Kresse, G. From Ultrasoft Pseudopotentials to the Projector Augmented-Wave Method. *Phys. Rev. B: Condens. Matter Mater. Phys.* **1999**, *59*, 1758−1775.
(51) Blöchl, P. E. Projector Augmented-Wave Method. *Phys. Rev. B: Condens. Matter Mater. Phys.* **1994**, *50*, 17953−17979.
(52) Methfessel, M.; Paxton, A. T. High-Precision Sampling for Brillouin-Zone Integration in Metals. *Phys. Rev. B: Condens. Matter Mater. Phys.* **1989**, *40*, 3616−3621.
(53) Kittel, C. *Introduction to Solid State Physics*; Wiley: New York, 2005.
(54) Tang, W.; Sanville, E.; Henkelman, G. A Grid-Based Bader Analysis Algorithm without Lattice Bias. *J. Phys.: Condens. Matter* **2009**, *21*, 84204.

DOI: 10.1021/acs.jpcc.6b11329
J. Phys. Chem. C 2017, 121, 10773−10780